A multi-technique tomography-based approach for non-invasive characterization of additive manufacturing components in view of

Dear Author,

Here are the proofs of your article.

- You can submit your corrections **online**, via **e-mail** or by **fax**.
- For **online** submission please insert your corrections in the online correction form. Always indicate the line number to which the correction refers.
- You can also insert your corrections in the proof PDF and **email** the annotated PDF.
- For fax submission, please ensure that your corrections are clearly legible. Use a fine black pen and write the correction in the margin, not too close to the edge of the page.
- Remember to note the **journal title**, **article number**, and **your name** when sending your response via e-mail or fax.
- **Check** the metadata sheet to make sure that the header information, especially author names and the corresponding affiliations are correctly shown.
- **Check** the questions that may have arisen during copy editing and insert your answers/ corrections.
- **Check** that the text is complete and that all figures, tables and their legends are included. Also check the accuracy of special characters, equations, and electronic supplementary material if applicable. If necessary refer to the *Edited manuscript*.
- The publication of inaccurate data such as dosages and units can have serious consequences. Please take particular care that all such details are correct.
- Please **do not** make changes that involve only matters of style. We have generally introduced forms that follow the journal's style.
  Substantial changes in content, e.g., new results, corrected values, title and authorship are not allowed without the approval of the responsible editor. In such a case, please contact the Editorial Office and return his/her consent together with the proof.
- If we do not receive your corrections **within 48 hours**, we will send you a reminder.
- Your article will be published **Online First** approximately one week after receipt of your corrected proofs. This is the **official first publication** citable with the DOI. **Further changes are, therefore, not possible.**
- The **printed version** will follow in a forthcoming issue.

Please note

After online publication, subscribers (personal/institutional) to this journal will have access to the complete article via the DOI using the URL: http://dx.doi.org/[DOI].
If you would like to know when your article has been published online, take advantage of our free alert service. For registration and further information go to: http://www.link.springer.com.

Due to the electronic nature of the procedure, the manuscript and the original figures will only be returned to you on special request. When you return your corrections, please inform us if you would like to have these documents returned.

Metadata of the article that will be visualized in OnlineFirst

ArticleTitle	A multi-technique tomography-based approach for non-invasive characterization of additive manufacturing components in view of vacuum/UHV applications: preliminary results	
Article Sub-Title		
Article CopyRight	The Author(s) (This will be the copyright line in the final PDF)	
Journal Name	Rendiconti Lincei. Scienze Fisiche e Naturali	
Corresponding Author	Family Name	**Grazzi**
	Particle	
	Given Name	**Francesco**
	Suffix	
	Division	Istituto Nazionale di Fisica Nucleare (INFN)
	Organization	Sezione di Firenze
	Address	Via G. Sansone 1, Sesto Fiorentino, 50019, Florence, Italy
	Division	
	Organization	Consiglio Nazionale delle Ricerche, Istituto di Fisica Applicata “Nello Carrara”
	Address	50019, Sesto Fiorentino, Italy
	Phone	
	Fax	
	Email	f.grazzi@ifac.cnr.it
	URL	
	ORCID	http://orcid.org/0000-0001-7255-6444
Corresponding Author	Family Name	**Giuntini**
	Particle	
	Given Name	**Lorenzo**
	Suffix	
	Division	Istituto Nazionale di Fisica Nucleare (INFN)
	Organization	Sezione di Firenze
	Address	Via G. Sansone 1, Sesto Fiorentino, 50019, Florence, Italy
	Division	Dipartimento di Fisica e Astronomia
	Organization	Università di Firenze
	Address	Via G. Sansone 1, Sesto Fiorentino, 50019, Florence, Italy
	Phone	
	Fax	
	Email	giuntini@fi.infn.it
	URL	
	ORCID	http://orcid.org/0000-0003-4563-2709
Author	Family Name	**Cialdai**
	Particle	
	Given Name	**Carlo**
	Suffix	

	Division	Istituto Nazionale di Fisica Nucleare (INFN)
	Organization	Sezione di Firenze
	Address	Via G. Sansone 1, Sesto Fiorentino, 50019, Florence, Italy
	Phone	
	Fax	
	Email	carlo.cialdai@fi.infn.it
	URL	
	ORCID	http://orcid.org/0000-0002-9062-8648
Author	Family Name	**Manetti**
	Particle	
	Given Name	**Marco**
	Suffix	
	Division	Istituto Nazionale di Fisica Nucleare (INFN)
	Organization	Sezione di Firenze
	Address	Via G. Sansone 1, Sesto Fiorentino, 50019, Florence, Italy
	Phone	
	Fax	
	Email	marco.manetti@fi.infn.it
	URL	
	ORCID	
Author	Family Name	**Massi**
	Particle	
	Given Name	**Mirko**
	Suffix	
	Division	Istituto Nazionale di Fisica Nucleare (INFN)
	Organization	Sezione di Firenze
	Address	Via G. Sansone 1, Sesto Fiorentino, 50019, Florence, Italy
	Phone	
	Fax	
	Email	massi@fi.infn.it
	URL	
	ORCID	http://orcid.org/0000-0002-0199-9296
Author	Family Name	**Morigi**
	Particle	
	Given Name	**Maria Pia**
	Suffix	
	Division	Dipartimento di Fisica e Astronomia “Augusto Righi”
	Organization	Università di Bologna
	Address	Viale Berti Pichat 6/2, 40127, Bologna, Italy
	Division	Istituto Nazionale di Fisica Nucleare (INFN)
	Organization	Sezione di Bologna
	Address	Viale Berti Pichat 6/2, 40127, Bologna, Italy
	Phone	
	Fax	
	Email	mariapia.morigi@unibo.it

	URL	
	ORCID	http://orcid.org/0000-0001-5697-2325
Author	Family Name	**Bettuzzi**
	Particle	
	Given Name	**Matteo**
	Suffix	
	Division	Dipartimento di Fisica e Astronomia “Augusto Righi”
	Organization	Università di Bologna
	Address	Viale Berti Pichat 6/2, 40127, Bologna, Italy
	Division	Istituto Nazionale di Fisica Nucleare (INFN)
	Organization	Sezione di Bologna
	Address	Viale Berti Pichat 6/2, 40127, Bologna, Italy
	Phone	
	Fax	
	Email	matteo.bettuzzi@unibo.it
	URL	
	ORCID	http://orcid.org/0000-0003-3464-6574
Author	Family Name	**Brancaccio**
	Particle	
	Given Name	**Rosa**
	Suffix	
	Division	Dipartimento di Fisica e Astronomia “Augusto Righi”
	Organization	Università di Bologna
	Address	Viale Berti Pichat 6/2, 40127, Bologna, Italy
	Division	Istituto Nazionale di Fisica Nucleare (INFN)
	Organization	Sezione di Bologna
	Address	Viale Berti Pichat 6/2, 40127, Bologna, Italy
	Phone	
	Fax	
	Email	rosa.brancaccio@unibo.it
	URL	
	ORCID	http://orcid.org/0000-0002-6240-5586
Author	Family Name	**Albertin**
	Particle	
	Given Name	**Fauzia**
	Suffix	
	Division	Dipartimento di Fisica e Astronomia “Augusto Righi”
	Organization	Università di Bologna
	Address	Viale Berti Pichat 6/2, 40127, Bologna, Italy
	Division	Istituto Nazionale di Fisica Nucleare (INFN)
	Organization	Sezione di Bologna
	Address	Viale Berti Pichat 6/2, 40127, Bologna, Italy
	Division	
	Organization	Study and Research Center Enrico Fermi
	Address	Piazza del Viminale 1, 00184, Rome, Italy

	Phone	
	Fax	
	Email	fauzia.albertin@unibo.it
	URL	
	ORCID	http://orcid.org/0000-0003-1983-1464
Author	Family Name	**Shinohara**
	Particle	
	Given Name	**Takenao**
	Suffix	
	Division	
	Organization	Japan Atomic Energy Agency
	Address	Tokai-mura, Naka-gun, Ibaraki, Japan
	Phone	
	Fax	
	Email	takenao.shinohara@j-parc.jp
	URL	
	ORCID	http://orcid.org/0000-0003-4432-7681
Author	Family Name	**Kai**
	Particle	
	Given Name	**Tetsuya**
	Suffix	
	Division	
	Organization	Japan Atomic Energy Agency
	Address	Tokai-mura, Naka-gun, Ibaraki, Japan
	Phone	
	Fax	
	Email	tetsuya.kai@j-parc.jp
	URL	
	ORCID	http://orcid.org/0000-0002-9892-4556
Author	Family Name	**Fedrigo**
	Particle	
	Given Name	**Anna**
	Suffix	
	Division	
	Organization	UKRI-STFC, ISIS Neutron and Muon Source
	Address	Oxfordshire, OX110QX, UK
	Phone	
	Fax	
	Email	anna.fedrigo@stfc.ac.uk
	URL	
	ORCID	http://orcid.org/0000-0002-1652-5608
Author	Family Name	**Giovanni**
	Particle	**Di**
	Given Name	**Adriano**
	Suffix	

	Division	
	Organization	New York University Abu Dhabi
	Address	Abu Dhabi, United Arab Emirates
	Phone	
	Fax	
	Email	adg11@nyu.edu
	URL	
	ORCID	http://orcid.org/0000-0002-8462-4894
Author	Family Name	**Arneodo**
	Particle	
	Given Name	**Francesco**
	Suffix	
	Division	
	Organization	New York University Abu Dhabi
	Address	Abu Dhabi, United Arab Emirates
	Phone	
	Fax	
	Email	francesco.arneodo@nyu.edu
	URL	
	ORCID	http://orcid.org/0000-0002-1061-0510
Author	Family Name	**Torres**
	Particle	
	Given Name	**Rodrigo**
	Suffix	
	Division	
	Organization	New York University Abu Dhabi
	Address	Abu Dhabi, United Arab Emirates
	Phone	
	Fax	
	Email	rodrigo.torres@nyu.edu
	URL	
	ORCID	
Author	Family Name	**Al-Ketan**
	Particle	
	Given Name	**Oraib**
	Suffix	
	Division	
	Organization	New York University Abu Dhabi
	Address	Abu Dhabi, United Arab Emirates
	Phone	
	Fax	
	Email	oga2@nyu.edu
	URL	
	ORCID	http://orcid.org/0000-0003-2736-3779
Author	Family Name	**Elhashemi**

	Particle	
	Given Name	**Jumaanah**
	Suffix	
	Division	
	Organization	New York University Abu Dhabi
	Address	Abu Dhabi, United Arab Emirates
	Phone	
	Fax	
	Email	jumaanah@nyu.edu
	URL	
	ORCID	http://orcid.org/0000-0001-9445-0923
Author	Family Name	**Taccetti**
	Particle	
	Given Name	**Francesco**
	Suffix	
	Division	Istituto Nazionale di Fisica Nucleare (INFN)
	Organization	Sezione di Firenze
	Address	Via G. Sansone 1, Sesto Fiorentino, 50019, Florence, Italy
	Phone	
	Fax	
	Email	francesco.taccetti@fi.infn.it
	URL	
	ORCID	http://orcid.org/0000-0003-2657-2990

Schedule	Received	5 April 2021
	Revised	
	Accepted	21 April 2021

Abstract	In this paper, we have studied an additively manufactured metallic component, intended for ultra-high vacuum application, the exit-snout of the MACHINA transportable proton accelerator beam-line. Metal additive manufacturing components can exhibit heterogeneous and anisotropic microstructures. Two non-destructive imaging techniques, X-ray computed tomography and Neutron Tomography, were employed to examine its microstructure. They unveiled the presence of porosity and channels, the size and composition of grains and intergranular precipitates, and the general behavior of the spatial distribution of the solidification lines. While X-ray computed tomography evidenced qualitative details about the surface roughness and internal defects, neutron tomography showed excellent ability in imaging the spatial density distribution within the component. The anisotropy of the density was attributed to the material building orientation during the 3D printing process. Density variations suggest the possibility of defect pathways, which could affect high vacuum performances. In addition, these results highlight the importance of considering building orientation in the design for additive manufacturing for UHV applications.

Keywords (separated by '-')	Selective laser melting (SLM) - X-ray computed tomography (XCT) - Neutron tomography (NT) - Non-destructive characterization - Microstructural analysis
Footnote Information	

Rendiconti Lincei. Scienze Fisiche e Naturali
https://doi.org/10.1007/s12210-021-00994-2

RESEARCH PAPER

A multi-technique tomography-based approach for non-invasive characterization of additive manufacturing components in view of vacuum/UHV applications: preliminary results

Francesco Grazzi[1,2] · Carlo Cialdai[1] · Marco Manetti[1] · Mirko Massi[1] · Maria Pia Morigi[3,4] · Matteo Bettuzzi[3,4] · Rosa Brancaccio[3,4] · Fauzia Albertin[3,4,5] · Takenao Shinohara[6] · Tetsuya Kai[6] · Anna Fedrigo[7] · Adriano Di Giovanni[8] · Francesco Arneodo[8] · Rodrigo Torres[8] · Oraib Al-Ketan[8] · Jumaanah Elhashemi[8] · Francesco Taccetti[1] · Lorenzo Giuntini[1,9]

Received: 5 April 2021 / Accepted: 21 April 2021

Abstract
In this paper, we have studied an additively manufactured metallic component, intended for ultra-high vacuum application, the exit-snout of the MACHINA transportable proton accelerator beam-line. Metal additive manufacturing components can exhibit heterogeneous and anisotropic microstructures. Two non-destructive imaging techniques, X-ray computed tomography and Neutron Tomography, were employed to examine its microstructure. They unveiled the presence of porosity and channels, the size and composition of grains and intergranular precipitates, and the general behavior of the spatial distribution of the solidification lines. While X-ray computed tomography evidenced qualitative details about the surface roughness and internal defects, neutron tomography showed excellent ability in imaging the spatial density distribution within the component. The anisotropy of the density was attributed to the material building orientation during the 3D printing process. Density variations suggest the possibility of defect pathways, which could affect high vacuum performances. In addition, these results highlight the importance of considering building orientation in the design for additive manufacturing for UHV applications.

Keywords Selective laser melting (SLM) · X-ray computed tomography (XCT) · Neutron tomography (NT) · Non-destructive characterization · Microstructural analysis

1 Introduction

Over the years, additive manufacturing (AM) (Ngo et al. 2018; Schmidt et al. 2017; Yap et al. 2015; Bourell et al. 2017), also known as 3D printing, and in particular metal AM (Debroy et al. 2018; Herzog et al. 2016; Du et al. 2016), has shown impressive growth, and 3D printing systems have constantly improved their performances in terms of dimensions of produced parts, precision, accuracy, and set of available materials.3D printing is constantly expanding its range of applications, and applications in fields unexpected in the past are becoming possible, ranging from cultural heritage (Taccetti et al. 2019) to radiation therapy (Woo 2016).One of the most used technologies in metal AM is the powder-based fusion (PBF) (Reevesinsight 2012). In the PBF process, the locally-released thermal energy melts the specific region of a powder bed, allowing the creation of complex solid objects. Generally, the PBF technologies used for metals are Selective Laser Melting (SLM), also known as direct metal laser sintering (DSLS), and electron beam melting (EBM) (Olsén et al. 2018). In SLM a laser source selectively bonds together powder particles layer-by-layer. In EBM technology, melting of metal powder is achieved with the use of a high-energy electron beam. The most extensively studied and used metal materials in AM techniques are steels, Al alloys, Ti alloys, and Ni superalloys (Wong and Hernandez 2012; Ferreri et al. 2020; Raj et al. 2019). Among steels, maraging steels are widely used in SLM, due to their good weldability linked to the lack of carbon (Turk et al. 2019). As detailed in the next paragraph, SLM technology applied to maraging steel has been used to produce the part studied in this paper.

✉ Francesco Grazzi
f.grazzi@ifac.cnr.it

✉ Lorenzo Giuntini
giuntini@fi.infn.it

Extended author information available on the last page of the article

In general, attractive features of AM are: the possibility of manufacturing small and complex components of lower mass than what achievable with conventional machining, lower material waste, a large variety of materials available, quick production implementation, reduced time for assembly/integration, easy prototyping to validate the solution, and good control over the chemical composition of the processed material. Despite the excellent capability in producing metal components with complex geometries, there are still some challenges in the dimensional accuracy of the produced parts as compared to the design. This can impose the need for post-processing operations in order to obtain components that are fully compliant with the design features. It is then important to rely on total-volume techniques to characterize metal AM parts, such as Neutron and X-ray diffraction and imaging techniques (Raj et al., 2019; Chae et al. 2019; Bao et al. 2020). In addition, non-destructive techniques allow the measured prototype to be used in the application for which it was designed.

Metal AM technology for ultra-high vacuum UHV applications is attracting growing interest both in companies and in the particle accelerator community. Studies dedicated to the in-vacuum characterisation of samples printed using metal AM technology have been presented, showing that these parts can be vacuum-compatible, and components built using metal AM qualify for their use in accelerators (Jenzer et al. 2019; Jenzer and Delerue 2019; Povilus et al. 2014).

However, the structure and morphology of metal AM parts depend strongly on process parameters (such as, but not limited to, temperature, scanning speed, material, powder size…). AM parts can present heterogeneous and anisotropic microstructures, very different from those shown in components produced with traditional technology, which can hinder the effectiveness for UHV applications, as they can result in unwanted internal features favoring outgassing, desorption, and permeation.

The accelerator beam-line of the MACHINA (Movable Accelerator for Cultural Heritage In-situ Non-destructive Analysis) project (Mathot et al. 2019) required the manufacturing of a special part to allow for beam extraction into atmosphere. The geometry of such components is too complex to be produced by standard machining, as multi-axial working systems are required. For this reason, it was produced using metal AM.

In order to acquire fabrication process-related microstructural information in connection with UHV performances, a non-invasive morphological and microstructural study of the MACHINA metal AM beam exit snout was performed using a combination of X-ray and Neutron Tomography (Maire and Withers 2014; Vontobel et al. 2006). Over the years, these techniques have been used on metal AM components (see for example (Thompson et al. 2017, 2016; Sacco and Moon 2019; Leung et al. 2018; du Plessis 2020) for X-ray CT and (Watkins et al. 2013; Cakmak et al. 2018; Brooks et al. 2018; Rahman et al. 2019; Hönnige et al. 2018) for Neutron Tomography) and less frequently together (see for example (Watkins et al. 2013)), since they can provide crucial information, as indicated e.g. in Perry et al. (2020).

This paper shows the potential of the combined NT and X-ray CT characterization of metal AM maraging-steel vacuum component produced using SLM. The obtained results will help to understand the relationships between production parameters and internal structures.

2 Materials and methods

2.1 The sample

The sample was produced using EOS Maraging Steel MS1 (Opatová et al. 2020). It is composed of two hollow cones with axes tilted 45° and intersecting at the tip, where the extraction window will be positioned. Details of the MACHINA exit snout and a rendering of the nozzle are reported in Fig. 1 (Giuntini et al. 2007).

Maraging steels possess superior strength and toughness without losing ductility, compared to common steel, and is preferred in special applications where UHV compliant materials are needed (LIGO Vacuum Compatible Materials List, LIGO-E960050-B-E, released by DCN E030570-01, 5 April 2004). Such materials mainly exhibit high strength and toughness. They show very little dimensional change when heat-treated, so they are often machined to the final dimensions and are quite suitable for the use in AM applications (Kempen et al. 2011; Hadadzadeh et al. 2020; Tan et al. 2017; Xu et al. 2018; Bodziak et al. 2019; Tewari et al. 2000).

The sample was made using the PBF-SLM technique with the EOS M280 AM printer. The machine uses a 400 W Ytterbium fibre laser, with beam diameter in the 100–500 μm range, and a scan speed up to 7 m/s. A 20 μm layer of EOS Maraging Steel MS1 powder was laid over a building plate using a coating blade, then a laser selectively melted the powder layer. A laser-contouring track is passed to solidify the borders of the part and a hatching track is used to solidify the interior. Between the layers, the direction of the laser passing in the hatching track keeps alternating. In order to optimize the layer deposition during the printing of the snout, the snout was oriented with the main axis tilted at 45° with respect to the horizontal plane and the vertical direction as shown in Fig. 2. In this way, the amount of removable support grid necessary for the correct growth of the snout is minimised, as well as the expected discontinuity effects between the main body and the 45° smaller tilted cone.

Journal : Large 12210 | Article No : 994 | Pages : 14 | MS Code : 994 | Dispatch : 4-5-2021

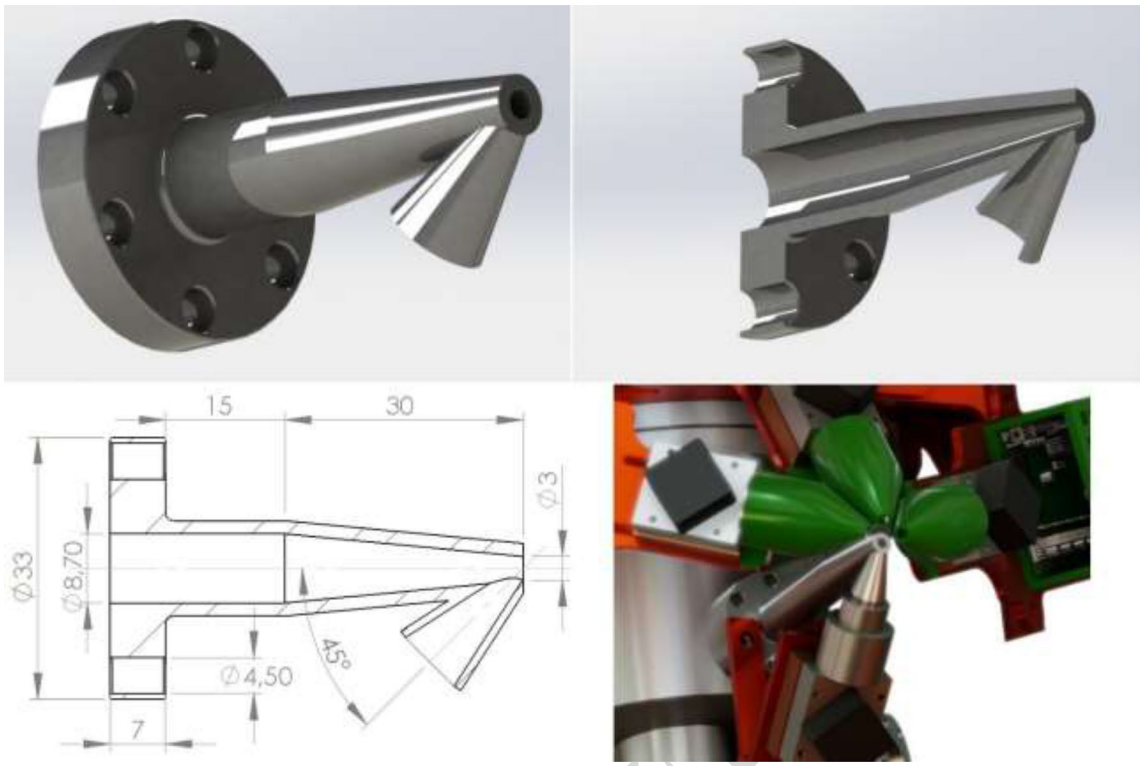

Fig. 1 The exit snout of the MACHINA beamline. Top: the exit snout (left) and its cross-section (right). The base of the nozzle is a standard DN16CF vacuum flange. Bottom: dimensional drawing (left) in mm and picture of the nozzle installed on the MACHINA beamline (right), with four X-ray detectors, three for element detection (with green conical caps) and one (below the nozzle) for counting the X-rays produced by the beam in the extraction window

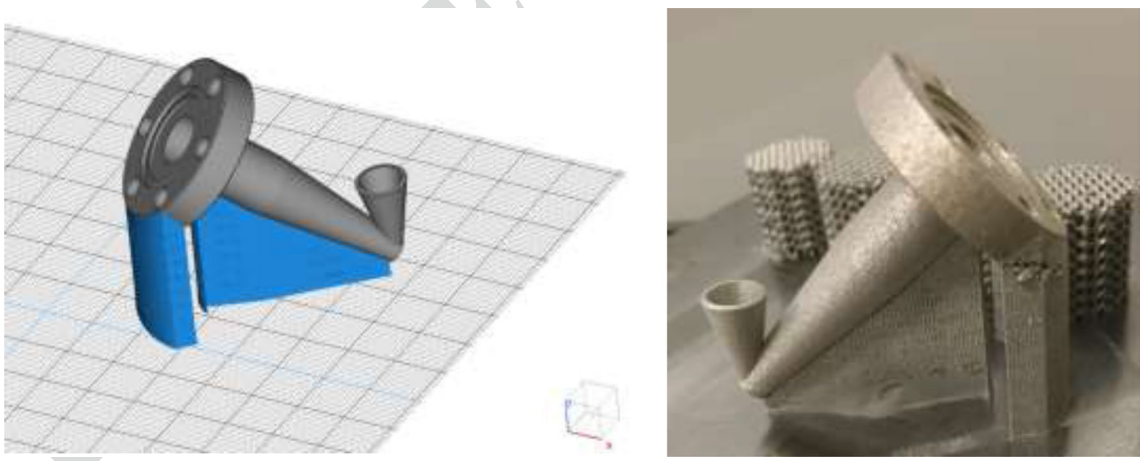

Fig. 2 (left) Model of the snout and of the support elements, showing the printing orientation. This configuration allowed us to grow the layers smoothly to complete the whole artefact. (right) The 3D printed sample as-built on the printing platform

The morphology of the as-received powder is shown in the SEM image of Fig. 3a. The ImageJ software (Schneider et al. 2012) was used to perform image analysis and obtain the size distribution of the powder. Results of the analysis of the particle size distribution are shown in Fig. 3b. Particle diameters range between 4 and 64 μm with a mean particle size of 21 μm and a standard deviation of 11 μm.

For vacuum applications, it is important to perform preliminary characterisation of the powder particle size and distribution, to correlate these features and the UHV

Journal : Large 12210 | Article No : 994 | Pages : 14 | MS Code : 994 | Dispatch : 4-5-2021

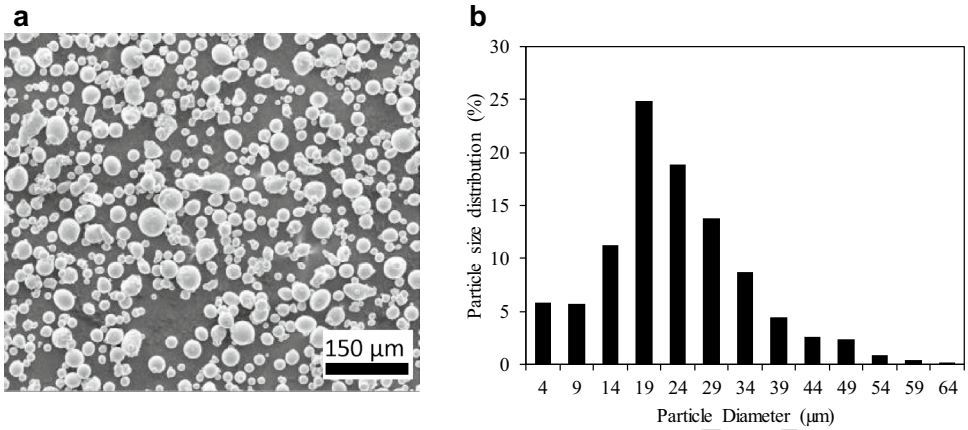

Fig. 3 SEM image of the Maraging-Steel powder used in the fabrication process of the nozzle

performances. The homogeneity of the resulting metal structure can indeed depend on the particle size.

2.2 Tomography analysis

The two tomographic methods, using X-ray and neutrons as probes, provide complementary results. In both cases, hundreds of transmission images (projections) are acquired at different angles by rotating the sample with respect to a fixed axis and are then converted into a 3D data set, composed of virtual slices describing the sample volume (Kak and Slaney 2001). The slices are generally represented in greyscale levels, where highly attenuating parts appear as bright areas and more transparent materials as dark ones.

2.2.1 X-ray tomography

X-ray computed tomography (XCT) is based on beam attenuation due to the interaction of X-ray with the atomic electrons of the sample investigated. Spatial resolution limitations in XCT are due to the detector pixel size, but when using X-ray tubes, the resolution also depends on the magnification and on the X-ray focal spot size (Martz et al. 2017; Bettuzzi et al. 2007). The XCT system used to scan the sample is the one at the INFN-CHNET X-ray Imaging Lab of the Department of Physics and Astronomy of Bologna University. The set-up is composed of a Varian PaxScan 2520D flat-panel X-ray detector (25×20 cm^2, 1536×1920 pixels, 127 µm pixel size, 1–10 fps, 14 bits ADC) and a Kevex PXS-10 micro-focus X-ray tube (130 kVp, 0.5 mA maximum current, 5 µm minimum focal spot size). The system is equipped with a precision two-axis horizontal-vertical translation stage for the detector, a vertical translation stage for the X-ray tube, and a micrometric rotation stage for the sample (Brancaccio et al. 2015, 2011; Morigi and Casali 2018).

Table 1 Scanning parameters in the two experimental configurations

	1st config	2nd config
Tube voltage	130 kV	130 kV
Tube current	90 µA	170 µA
Beam filtration	0.2 mm Fe	0.5 mm Pb
Detector frame rate	2 fps	2 fps
Frame average	4	4
Number of projections	900	900
Angular range	360 deg	360 deg
Detector pixel size	127 µm	127 µm
Source-detector distance	729 mm	729 mm
Source-object distance	223.5 mm	223.5 mm
Object-detector distance	505.5 mm	505.5 mm
Magnification	3.26	3.26
Voxel size	39 µm	39 µm

Table 1 reports the parameters of the two experimental configurations for the sample scan. The first scan was optimized for the thinner part of the sample while the second for the thicker one. Moreover, in the latter, the specimen's main axis was tilted of almost 45° with respect to the support base in order to minimize the reconstruction artefacts. In the second configuration, the beam was also filtered with 0.5 mm lead sheet, to remove the low-energy X-rays to minimize beam-hardening artefacts.

2.2.2 Neutron tomography

Neutron Tomography (NT), on the contrary, is based on beam attenuation due to a combination of scattering and absorption by the target nuclei (the relative weight of the two phenomena depends on the atomic species and the crystal structure) (Sears 1992). The combination between the lower incoming beam collimation and the sample scattering effect reduces the

Journal : Large 12210 | Article No : 994 | Pages : 14 | MS Code : 994 | Dispatch : 4-5-2021

transmitted beam collimation and the neutron radiographies are then more blurred than those obtained using X-rays (Bilheux et al. 2009). For this reason samples for NT are generally placed as close as possible to the detector, thus achieving no image magnification. In general, for most dense materials, the penetration power of neutrons used in NT is much higher than that of X-rays used in XCT, so that microstructural features related to the crystalline structure inside the sample volume can be highlighted.

NT has a spatial resolution generally varying between 20 and 250 μm, depending on the experimental configuration, and allows for evidencing possible variations of density in the bulk (even bubbles and cracks), thanks to the different attenuation coefficients of volumes of different density (Bilheux et al. 2009). Moreover, since neutron beam attenuation is related to absorption and coherent and incoherent scattering, it is possible to exploit the coherent scattering attenuation effect (Lovesey 1986), to observe microstructural features of the crystalline grains. In fact, the attenuation power of coherent scattering is related to the size of crystallographic domains, to the presence of preferential orientations, and to the compositional discrepancies (52 Santisteban et al. 2001).

Neutron imaging performed using cold neutrons (wavelength from 3 Å on) represents the best option to maximize material contrast from coherent scattering. The typical cold neutron beam has high flux in the wavelength range between 3 and 5 Å, which corresponds to the region where diffraction effects on the transmitted beam exhibit the maximum contrast (Santisteban et al. 2001; Kaestner et al. 2011).

The NT measurements shown in this work were taken at the RADEN beam-line (Shinohara et al. 2016, 2020) at the MLF J-PARC (JPARC 2021) spallation neutron source in Japan, an imaging beam-line with a wide thermal and cold neutron wavelength range (1.8–6.8 Å). The experimental parameters are reported in Table 2.

The sample was wrapped in aluminum foil and fixed into a thin aluminum tube, mounted on a rotating stage, to allow for an easy sample positioning on the beam-line.

Data processing was performed using both ImageJ 42 (Schneider et al. 2012) and Octopus 57 (Vlassenbroeck et al. 2006) software. Since accelerator-based neutron source can show some intensity fluctuations (these sources are known to be slightly less stable than reactors 58 (Windsor 1981)), flux variations were accounted for using an area of the projections where no sample was present at all angles. The tomography slices were then rotated to align the main geometrical axes of the sample to the x–y–z orientation of the slices, to better correlate the sample geometry with the observed morphological and microstructural effects.

3 Results

3.1 X-rays results

For both X-ray tomographic configurations (see Table 1 for details), the achieved voxel size is around 40 μm. Figure 4 shows a 3D rendering of the upper part of the object with (a) a frontal plane cutting the reconstructed volume and (b) the corresponding virtual section. It is clear from the figure that the internal surface of the component is quite rough. By looking at the cross-section of the cone, it is also possible to observe the presence of inhomogeneous porosity inside the volume of the walls. A close-up of the cone wall, highlighted by the red rectangle, allows observing the shape, size, and distribution of the pores.

Figure 5 shows a sagittal section of the sample and the corresponding tomography slice. The bottom-right corner shows a detail of the section, highlighting the roughness of the internal surface. Considering that the sample was grown by printing it along a tilted axis (see Fig. 2), the observed channel-like structure, on the inner surface, suggests that the growth of a layer is influenced by the spatial arrangement of the previous ones. The roughness of the internal surface also originates from loose powder just partially adhering. The connection between the cones appears free from flaws and defects, even though it is possible to spot the presence of a few pores.

Figure 6 shows two axial sections taken at different heights of the cone. In both of them, the irregular and rough internal surface is visible. The wall shows strong beam hardening effects.

The second X-ray scan was performed minimizing reconstruction artefacts (generated by strong attenuation and beam hardening effects). The scan allowed us to obtain limited information on the coarse structure of the material and the surface alterations of this part of the sample. It has been possible to visualise the irregular internal surface of all the screw holes of the base, as shown in Fig. 7. The apparent density fluctuations and the weak diagonal bands in the bulk of the base are reconstruction artefacts due to beam hardening.

Table 2 Summary of the experimental conditions for the NT. L/D represents the source to detector distance L over the pinhole diameter D

L/D	Field of view	Resolution	#projections	Acquisition time per projection	#Number of tomographies
400	52×52 mm	70 μm	720	30 s	2

Journal : Large 12210 | Article No : 994 | Pages : 14 | MS Code : 994 | Dispatch : 4-5-2021

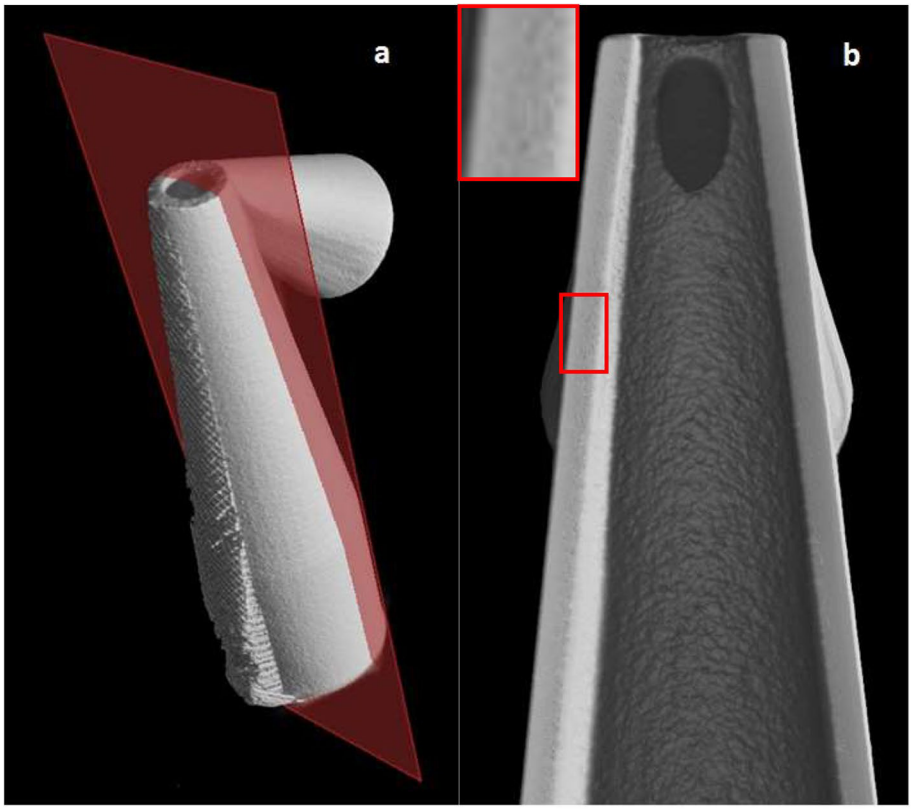

Fig. 4 **a** Virtual cut with a frontal plane of the 3D rendering of the conical element of the sample. **b** Frontal section of the upper part of the sample showing the internal rough surface of the conical element and the elliptical intersection between the two cones. Magnification of the red highlighted area showing the presence of pores is reported in the top left corner

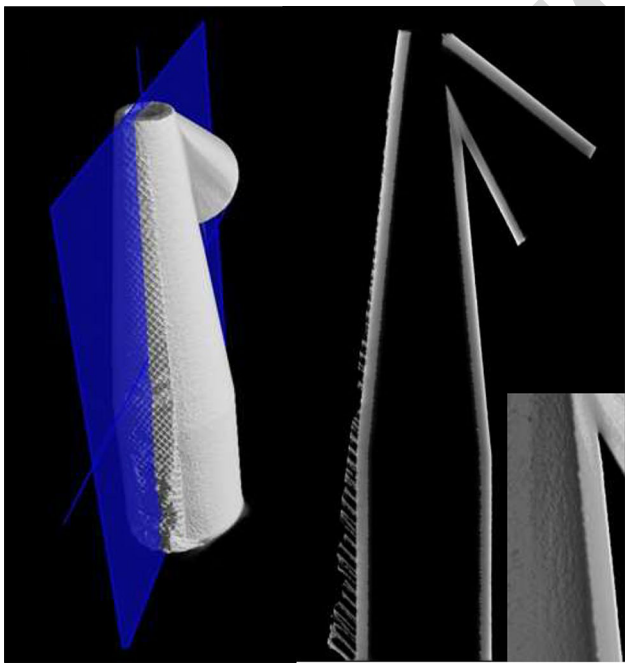

Fig. 5 Left-hand side, sagittal section of the reconstructed volume of the sample; right-hand side, sagittal slice, and detail of the sliced volume at the joint between the two cones. The joint, which can be a critical point, appears flawless. As in the previous figure, the internal surface appears rough

3.2 Neutron tomography results

The neutron investigation allowed identifying several interesting microstructural features. Since there is no macroscopic compositional variation across the sample, variation in attenuation coefficients are solely due to the different density or coherent scattering power from the grains. In general, solid metal microstructural features and cavities, with dimensions down to a few hundred microns, can be easily visualized with NT over depths of several centimeters. It was possible to visualize the porosity distribution in the sample. The anisotropic distribution of the pores in the nozzle base (a DN16CF flange, about 33 mm outer diameter, see Fig. 1 for all the details) is clearly visible in tomography slices. In Fig. 8, the porosity distribution on a frontal section is evidenced. The thick cylindrical base is highly porous, with large parts of the volume showing a lower attenuation coefficient indicating higher porosity. This effect is particularly visible in the volume around the hollow central part.

In addition, the component shows a strong asymmetry in porosity distribution between the left- and the right-hand side. At the base, porosity is distributed along a diagonal ellipsoidal volume and this distribution is possibly correlated with the diagonally arranged printing direction of the sample, as shown in Fig. 2. Along the conical nose, pores are more densely distributed on the right-hand side. A light grey layer is present along most of its surface. This is an effect

Journal : Large 12210 | Article No : 994 | Pages : 14 | MS Code : 994 | Dispatch : 4-5-2021

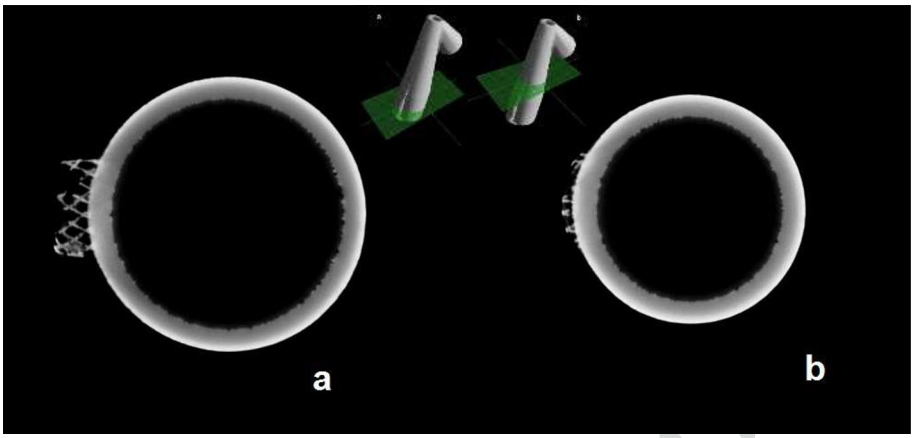

Fig. 6 Axial slices at two different heights of the sample. **a** Close to the base; **b** at about half-length of the cone. Both axial sections show the internal irregular surface and the beam hardening effect

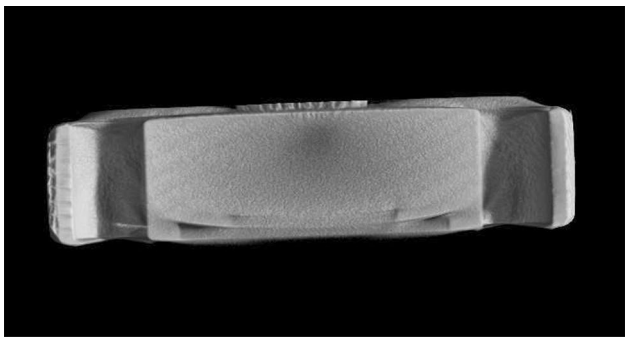

Fig. 7 Frontal section of the base on the reconstructed 3D volume showing the irregular inner surface of the holes

induced by the increased scattering phenomenon due to the application of shot peening surface finishing, which reduces the average grain size (connected with the size of the crystallographic domains) and slightly increases the density, thus increasing the general attenuation power of the area. It is possible to exploit this analysis to measure the effectiveness (by the different grayscale attenuation) and the penetration depth of shot peening treatment.

In Fig. 9, a sagittal section of the base is shown, a few mm away from of the hole side, eccentric with respect to the central axis, 90° rotated with respect to Fig. 8. The anisotropic distribution of the porosity shows abrupt density variations where the most porous area surrounds the

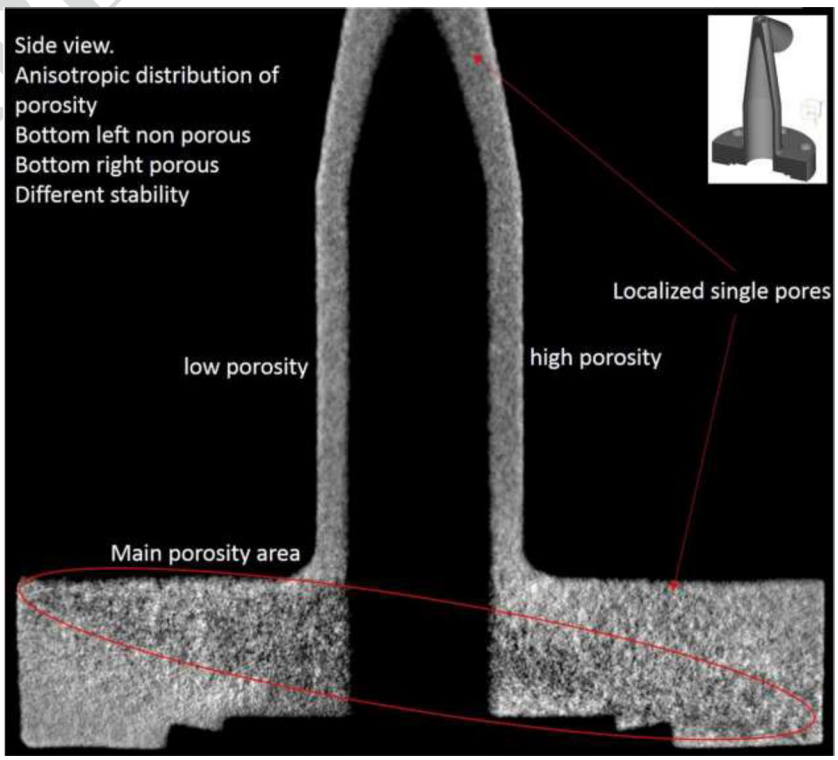

Fig. 8 Frontal section of the MACHINA exit snout. The anisotropic distribution of the porous areas in the different parts is clearly visible

Journal : Large 12210 | Article No : 994 | Pages : 14 | MS Code : 994 | Dispatch : 4-5-2021

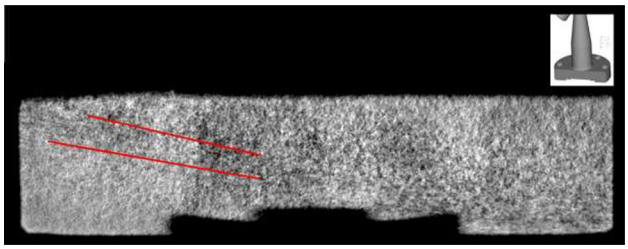

Fig. 9 Sagittal view of the base, eccentric with respect to the central hole. Red lines on the left are a guide to show some preferred orientations of the directional solidification. On the bottom left side, randomly distributed, light grey reticulated lines are also visible. They show the presence of inter-granular precipitation and appear light due to the presence of cobalt

central hole. With such high porosity, which appears to form a network, the pores may create a (partial) pathway connecting the inner (i.e. in vacuum) and the outer (i.e. in atmosphere) side of the snout. Red lines in Fig. 9 are a guide to the eye to evidence structures related to coherent-scattering neutron attenuation. These structures indicate the presence of preferred orientations of the grains, correlated to directional solidification, which appears to be non-parallel, ascribable to the sample orientation during the print.

Light grey randomly reticulated lines show the presence of inter-granular precipitation. They are particularly evident at the left-hand side, just below the red lines. The precipitates must be rich in cobalt since it is present in the alloy. Cobalt is an element that strongly attenuates neutrons and Co-rich areas appear bright in the slice.

Figure 10 shows another frontal view, parallel to Fig. 8. The anisotropic distribution of porosity is evident, both radially (with respect to the central hole) and diagonally (with respect to the base). Solidification lines are also visible in the cylindrical part of the nose and appear diagonally tilted, as evidenced by the red line. Other inhomogeneities are visible in the base, indicating different relative concentrations of the alloying elements of the steel and the presence of a network of precipitates with different concentration and size. This means that the heating induced by the SLM procedure has local and areal effects, related to the sample geometry, machine speed, and other factors, which might affect the mechanical characteristics of the sample. The abrupt change of density and microstructure between the thick base and the thin walls of the nose is also evident.

Figure 11 shows another frontal cross-section and offers a different view of both the porosity distribution and solidification directions. The different effects induced by shot peening are very clear when looking at the top arch, where bright and dark grains are visible. Geometric deformations within the screwing holes in the base are also visible (left-hand side tilted with respect to the external side face, right-hand side

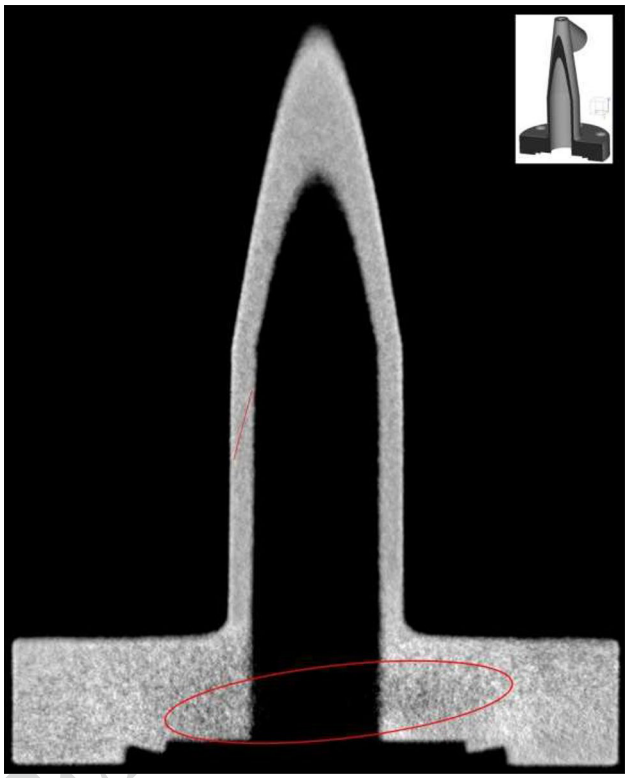

Fig. 10 Frontal view. It is evident the anisotropic distribution of porosity (as highlighted by the red oval) and the presence, in the nose, of highly tilted solidification lines, as highlighted by the red line on the left

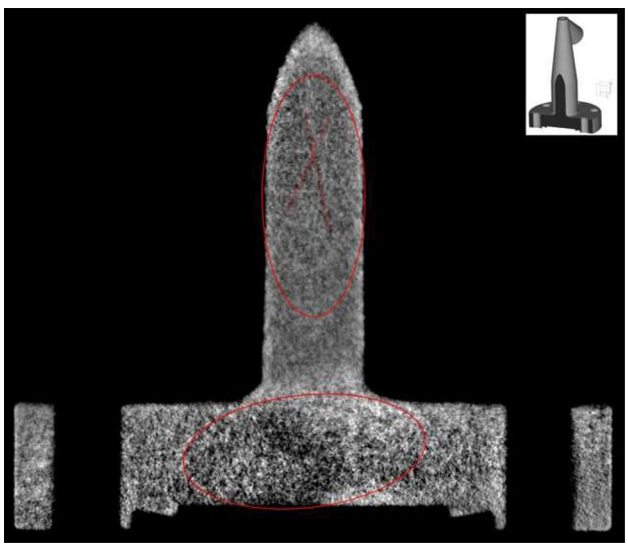

Fig. 11 Frontal cross-section, parallel to Fig. 10, showing the porosity distribution and the complex network of the solidification lines. Geometric deformation within the screwing holes in the base are also visible (left-hand side tilting with respect to the external side face, right-hand side bent banana shape effect)

Journal : Large 12210 | Article No : 994 | Pages : 14 | MS Code : 994 | Dispatch : 4-5-2021

bent with banana-shape effect), a macroscopic effect in the millimeter scale.

Figure 12 shows an axial view of the top head of the connector. On the main circular element, the surface treatment induced by shot peening is evident, which is more effective on the top half. The red lines show a grid correlated to the solidification directions, which follow different orientations and density distributions, according to the different areas along the circumference. The elliptical element is a section of the tilted cone and shows an average lower density and higher porosity in the bottom half. The volume of the connecting part between the cones shows a strong variation of attenuation coefficients and directional solidification lines, but no pores. This is not a foregone result, due to the complex geometry of this part of the nozzle, and confirms that the metal AM technology can be a proper approach to the production of complex parts not only for mechanical components but also for accelerators.

Figure 13 shows a lower axial slice with respect to Fig. 12, closer to the base. The red lines show a grid correlated to the solidification directions, following different orientations and distributions according to their positions within the sample. The rim of the tilted conical element (bottom in the figure) exhibits a different attenuation coefficient on the very edge. Some pores are evident throughout the section. The typical tomography reconstruction ring artefacts are visible on the central area of the left side of the tilted cone, showing completely different behavior with respect to the solidification lines, thus demonstrating that solidification lines are real effects.

Figure 14 shows a frontal view of the connecting area between the vertical and tilted cone. The distribution of the solidification lines all along the section is evident. The intersection volume appears quite homogenous, confirming the conclusions of Fig. 12, and shows little porosity or microstructural effects induced by the geometry. As expected, the inner

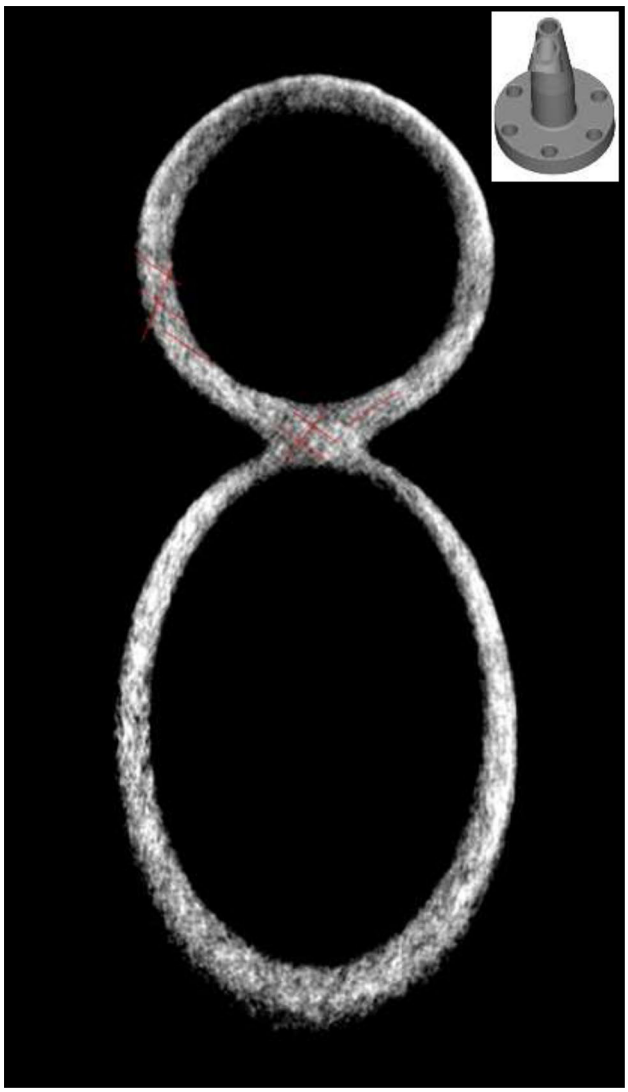

Fig. 12 Axial section view of the conical connectors, including their superimposition volume. The solidification line grid is visible, as evidenced by the crossed red lines

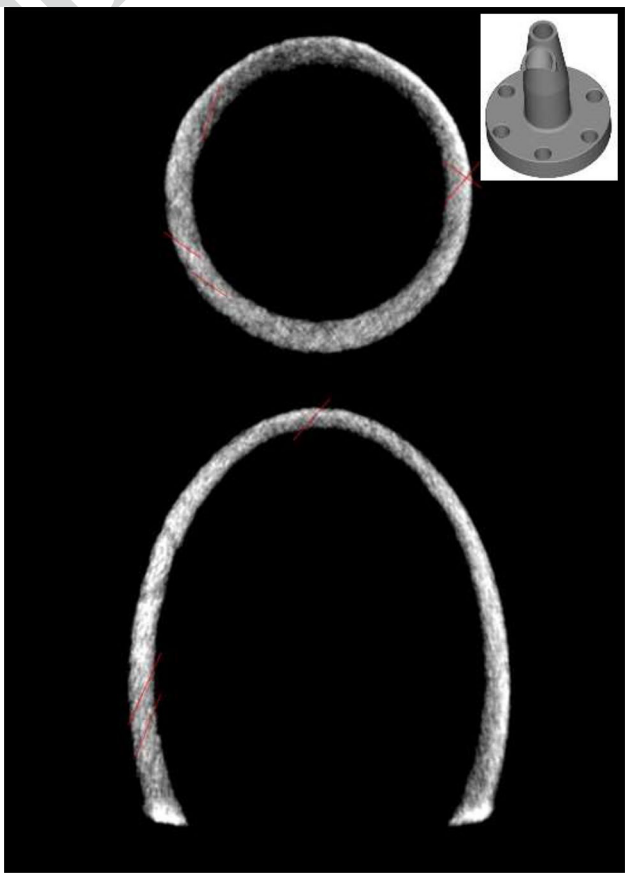

Fig. 13 Lower section view of the conical connectors. Solidification line grid is visible

Journal : Large 12210 | Article No : 994 | Pages : 14 | MS Code : 994 | Dispatch : 4-5-2021

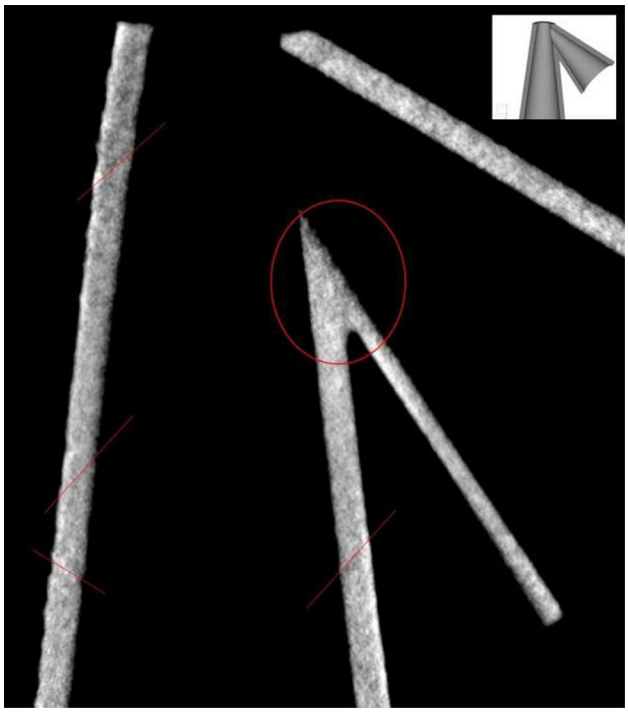

Fig. 14 Frontal view of the volume connecting the vertical and the tilted cones. Solidification lines are visible. Nevertheless, the connecting volume appears sound metal, even though it shows small microstructural variations

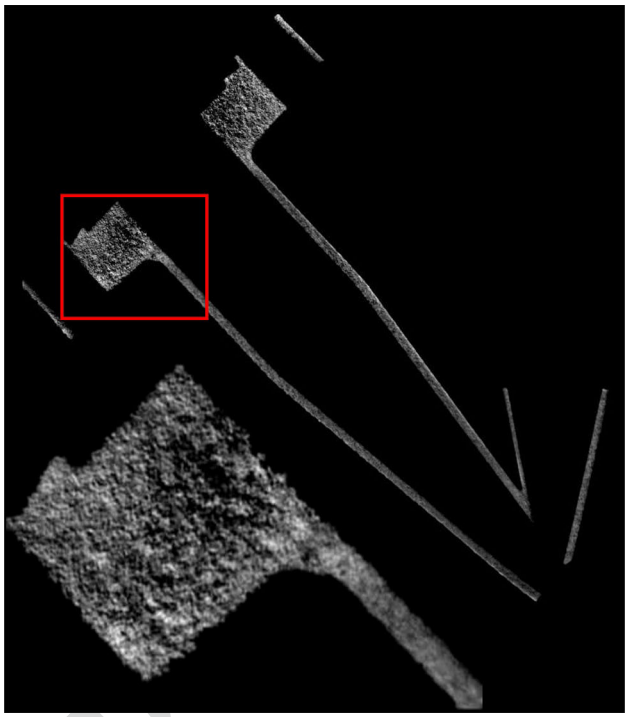

Fig. 15 Frontal view tomography slice with the sample shown in as-grown orientation. It is evident the presence of a horizontal discontinuity in the grey tones of the thin hollow cylinder, in the red squared area, and in the magnified image on the bottom left. Since the printing started with two independent pieces, unified for the first time at this height, the different thermal history gives origin to a discrepancy in the microstructure and orientation

surface of the cones appears uneven, since no shot peening surface treatment was applied there.

Figure 15 shows a further effect revealed by neutron tomography. The sample was printed tilted at 45°, therefore it started to be printed in two separate parts (see Fig. 2). When the part coming from the thick base and the one from the thin wall of the cylinder, having an independent thermal history and grain orientation, come into contact, it is possible to expect discontinuity effects. In fact, the grayscale tones of the two parts appear different, lighter in the basement disk and darker in the thin cylinder. Moreover, there is a clear horizontal discontinuity in the attenuation coefficient of the cylinder. This is possibly due to a forced reorientation of the grains induced in the thin wall by the more massive disk element. The laser heating during the deposition of the layers could cause a sort of annealing phenomenon in the less massive part, changing its microstructural orientation. This means that the heating effect could induce the re-arrangement, under specific conditions, even in the layers already printed before the connection took place.

4 Discussion

Data analysis provided quantitative results in terms of dimensional and microstructural features, shortly summarised hereafter.

From XCT data, it has been possible to:

1. Carry out the dimensional analysis of the several elements of the snout, such as wall thickness and curvature, which turned out to be compliant with the design specifications within 100 µm tolerance, mainly due to surface roughness.
2. Determine the surface roughness, which resulted to be below 40 µm (limit of resolution, set by pixel size).
3. Estimate the dimension of the porosity, observed in the walls of the snout, which resulted to be in the 100–300 µm scale.
4. Point out the excellent quality (almost flaw-less) of the material in the volume connecting of the two conical elements.
5. Observing the presence of non-negligible distortions (up to the 200–300 µm scale) in the screw-passing holes of the base.

The lack of information about the bulk structure in the metal and the possible presence of microstructural

Journal : Large 12210 | Article No : 994 | Pages : 14 | MS Code : 994 | Dispatch : 4-5-2021

distortions, excluding the effect of reconstruction artefacts, confirmed the need of a higher penetrating probe, whose interaction is not mainly based on absorption, as is the case XCT.

NT data analysis confirmed the excellent capability of cold neutrons to identify microstructural and compositional features within solid metal. In this specific sample, several important features were identified:

1. Porosity size (ranging from 150 µm diameter, the resolution limit, up to 300 µm).
2. Porosity shape and spatial distribution (smaller holes in the snout walls, bigger in the base, where a noticeable and unexpected decrease of density is evident).
3. Microstructural effects of shot peening treatment. It was possible to measure its local effect resulting in a reduction of the grain size (decrease of neutron transmission induced by the increase of the scattering power due to the smaller size of the grains and the increase of the local density of defects).
4. The depth of the shot-peening treatment, which is about 200 µm.
5. Qualitative determination of size and shape of the grains, pointed out by a non-homogeneous spatial distribution of inter-granular Co-rich precipitates (in the NT images, a paler reticulate caused by a higher Co presence at the grain boundaries. This higher Co presence is induced by the thermal effects of the additive manufacturing process).
6. The general behavior of the spatial distribution of the solidification lines. It was evidenced that they diagonally intersect the external walls and that the general shape of the grains along the nose walls follow the main growth directions and sometimes exhibit arch-shaped features. These arches are generated by the solidification directions during the additive manufacturing process, following thermal gradients and adduction directions.
7. The presence of a discontinuity in the microstructure caused by the unification of two parts (the thick base and the thin wall of the cylinder). Because of the orientation, they are initially printed as separate parts and thus experience different thermal histories and grain orientations before joining. These different thermal histories and grain orientations caused, during the joining process, the microstructural discontinuities evidenced by NT.

Considering that only non-invasive techniques have been used, the level of characterization of the analyzed sample is highly satisfactory in terms of microstructural and dimensional analysis.

5 Conclusions

For accelerator science and in general, for UHV applications, there is a strong interest in exploiting metal AM production processes for prototyping and production of special components. To point out possible relationships between metal AM machine configurations and UHV performances, it is necessary the availability of non-destructive techniques (Fernandez et al. 2020) able to provide microstructural information about the parts of interest, possibly being able to point out also the differences between parts produced with metal AM and conventional machining. We performed such a study on the exit snout of MACHINA, the first transportable particle accelerator. We used two non-destructive imaging techniques, XCT and NT, to investigate the resulting microstructure of the exit snout, additively manufactured out of Maraging steel.

XCT evidenced qualitative details about the surface roughness and internal defects, NT showed excellent ability in imaging the spatial density distribution within the component. In addition, NT allowed us to correlate the internal density distribution with the building orientation of the part. Density variations suggest the possibility of defect pathways, which could affect high vacuum performances. In addition, these results highlight the importance of considering building orientation in the design for additive manufacturing for UHV applications.

Further investigations are needed to characterize precipitates, distortion, and other features, possibly with the addition of neutron and X-ray diffraction (Merlino 2013; Allegra 2013; Artioli 2013; Dabagov et al. 2020). Furthermore, a full UHV characterization on purposely-prepared metal AM vacuum parts is also necessary. This research program is already in progress.

Acknowledgments The authors wish to warmly thank the PRISMA association (www.prisma-cultura.it), and in particular Nicola Amico, for the precious collaboration in the preparation of Figure 1. This research was partially carried out using the Core Technology Platforms resources at New York University Abu Dhabi.

Author contributions Conceptualization: LG, FG, MM, CC, and FT; methodology and writing—original draft preparation: LG, FG, MM, FT, MM, FA, RT, OAK, and JE; CAD design: MM, CC; 3D metal print: FA, ADG, RT, OAK, and JE; neutron irradiation, neutron imaging, and neutron data analysis: FG, LG, AF, MM, TS, and TK; X-ray irradiation, X-ray imaging, and data analysis: FA, RB, MB, and MPM; paper review and editing: LG, FG, AF, MM, OAK, and JE.

Funding Open access funding provided by Università degli Studi di Firenze within the CRUI-CARE Agreement. Not applicable.

Declarations

Conflicts of interest The authors declare that they have no known competing financial interests or personal relationships that could have appeared to influence the work reported in this paper.

References

Allegra G (2013) From X-ray, neutron diffraction and molecular modelling to the crystalline structure of stereoregular polymers: a concise outlook. Rend Fis Acc Lincei 24:63–70. https://doi.org/10.1007/s12210-013-0222-8

Artioli G (2013) Science for the cultural heritage: the contribution of X-ray diffraction. Rend Fis Acc Lincei 24:55–62. https://doi.org/10.1007/s12210-012-0207-z

Bao J, Wu S, Withers PJ, Wu Z, Li F, Fu Y, Sun W (2020) Defect evolution during high temperature tension-tension fatigue of SLM AlSi10Mg alloy by synchrotron tomography. Mater Sci Eng A 792:139809. https://doi.org/10.1016/j.msea.2020.139809

Bettuzzi M, Brancaccio R, Casali F, Morigi MP (2007) Effective dynamic range measurement for a CCD in full–field industrial X–ray imaging applications. Proc SPIE Opt Meas Syst Ind Inspect 6616:66161L. https://doi.org/10.1117/12.726165

Bodziak S, Al-Rubaie KS, Dalla-Valentina L, Humel-Lafratta F, Costa-Santos E, Marcon-Zanatta A, Chen Y (2019) Precipitation in 300 grade maraging steel built by selective laser melting: aging at 510 °C for 2 h. Mater Char 151:73–83. https://doi.org/10.1016/j.matchar.2019.02.033

Bourell D, Kruth JP, Leu M, Levy G, Rosen D, Beese AM, Clare A (2017) Materials for additive manufacturing. CIRP Ann 66:659–681. https://doi.org/10.1016/J.CIRP.2017.05.009

Brancaccio R, Bettuzzi M, Casali F, Morigi MP, Levi G, Gallo A, Marchetti G, Schneberk D (2011) Real-time reconstruction for 3-D CT applied to large objects of cultural heritage. Nucl Sci IEEE Trans 58:1864–1871. https://doi.org/10.1109/TNS.2011.2158850

Brancaccio R, Bettuzzi M, Casali F, Morigi MP, Ragazzini L (2015) Image quality and dose assessment in inner ear computed tomography imaging with a flat panel–based system. J Comput Assist Tomogr 39:232–295. https://doi.org/10.1097/RCT.0000000000000176

Brooks AJ, Yao H, Yuan J, Kio O, Lowery CG, Markötter H, Kardjilov N, Guo S, Butler LG (2018) Early detection of fracture failure in SLM AM tension testing with Talbot-Lau neutron interferometry. Addit Manuf 22:658–664. https://doi.org/10.1016/j.addma.2018.06.012

Cakmak E, Sridharan N, Venkatakrishnan SV, Bilheux HZ, Santodonato LJ, Shyam A, Babu SS (2018) Feasibility study of making metallic hybrid materials using additive manufacturing. Metall Mater Trans A 49:5035–5041. https://doi.org/10.1007/s11661-018-4741-x

Chae H, Huang EW, Jain J, Wang H, Woo W, Chen S-W, Harjo S, Kawasaki T, Lee SY (2019) Plastic anisotropy and deformation-induced phase transformation of additive manufactured stainless steel. Mater Sci Eng A 762:138065. https://doi.org/10.1016/j.msea.2019.138065

Dabagov SB, Hampai D, Guglielmotti V et al (2020) X-ray applications and recent advances @ XLab Frascati. Rend Fis Acc Lincei 31:443–453. https://doi.org/10.1007/s12210-020-00903-z

Debroy T, Wei HL, Zuback JS, Mukherjee T, Elmer JW, Milewski JO, Beese AM, Wilson-Heid A, De A, Zhang W (2018) Additive manufacturing of metallic components—process, structure and properties. Prog Mater Sci 92:112–224. https://doi.org/10.1016/j.pmatsci.2017.10.001

Du J, Wei Z, Wang X, Zhao G (2016) A novel high-efficiency methodology for metal additive manufacturing. Appl Phys A 122:945. https://doi.org/10.1007/s00339-016-0480-2

du Plessis A, Yadroitsava I, Yadroitsev I (2020) Effects of defects on mechanical properties in metal additive manufacturing: a review focusing on X-ray tomography insights. Mater Des 187:108385. https://doi.org/10.1016/j.matdes.2019.108385

Fernandez JE, Taccetti F, Kenny JM et al (2020) Conclusive editorial on non-destructive techniques for cultural heritage. Rend Fis Acc Lincei 31:819–820. https://doi.org/10.1007/s12210-020-00937-3

Ferreri NC, Vogel SC, Knezevic M (2020) Determining volume fractions of γ, γ′, γ″, δ, and MC-carbide phases in Inconel 718 as a function of its processing history using an advanced neutron diffraction procedure. Mater Sci Eng A 781:139228. https://doi.org/10.1016/j.msea.2020.139228

Giuntini L, Massi M, Calusi S (2007) The external scanning proton microprobe of Firenze: a comprehensive description. Nucl Instr and Meth A 576:266–273. https://doi.org/10.1016/j.nima.2007.03.021

Hadadzadeh A, Shahriari A, Amirkhiz BS, Li J, Mohammadi M (2020) Additive manufacturing of an Fe–Cr–Ni–Al maraging stainless steel: microstructure evolution, heat treatment, and strengthening mechanisms. Mater Sci Eng, A 787(10):139470. https://doi.org/10.1016/j.msea.2020.139470

Herzog D, Seyda V, Wycisk E, Emmelmann C (2016) Additive manufacturing of metals. Acta Mater 117:371–392. https://doi.org/10.1016/j.actamat.2016.07.019

Hönnige J, Colegrove PA, Ganguly S, Eimer E, Kabra S, Williams S (2018) Control of residual stress and distortion in aluminium wire+ arc additive manufacture with rolling. Addit Manuf 22:775–783. https://doi.org/10.1016/j.addma.2018.06.015

Jenzer S, Delerue N (2019), Prospects of additive manufacturing for accelerators. In: 10th Int. Particle Accelerator Conf. IPAC2019, Melbourne, Australia JACoW Publishing, ISBN: 978-3-95450-208-0. https://doi.org/10.18429/JACoW-IPAC2019-THPTS008

Jenzer S, Alves M, Bilgen S, Bonis J, Brisset F, Djelali S, Gonnin A, Guerrier M, Grasset D, Letellier-Cohen F, Mercier B, Mistretta E, Sattonnay G (2019) Is it possible to use additive manufacturing for accelerator UHV beam pipes? J Phys Conf Ser 1350:012199. https://doi.org/10.1088/1742-6596/1350/1/012199

JPARC (2021) https://j-parc.jp/MatLife/en/index.html. Accessed 29 Mar 2021

Kaestner AP, Hartmann S, Kühne G, Frei G, Grünzweig C, Josic L, Schmid F, Lehmann EH (2011) The ICON beamline—a facility for cold neutron imaging at SINQ. Nucl Instr Meth Phys Res A 659:387–393. https://doi.org/10.1016/j.nima.2011.08.022

Kak AC, Slaney M (2001) Principles of computerized tomographic imaging, society of industrial and applied mathematics

Kempen K, Yasa E, Thijs L, Kruth JP, van Humbeeck J (2011) Microstructure and mechanical properties of selective laser melted

AQ3

18Ni-300 steel. Phys Procedia 12:255–263. https://doi.org/10.1016/j.phpro.2011.03.033

Leung CLA, Marussi S, Atwood RC, Towrie M, Withers PJ, Lee PD (2018) In situ X-ray imaging of defect and molten pool dynamics in laser additive manufacturing. Nat Commun 9:1355. https://doi.org/10.1038/s41467-018-03734-7

Lovesey SW (1986) Theory of neutron scattering from condensed matter, vol 1, Nuclear scattering. Oxford Science Publications, Oxford

Maire E, Withers PJ (2014) Quantitative X-ray tomography. Int Mater Rev 59:1–43. https://doi.org/10.1179/1743280413Y.0000000023

Martz HE Jr, Logan CM, Schneberk DJ, Shull PJ (2017) X-ray imaging. Fundamentals, industrial techniques and applications. CRC Press, Boca Raton. https://doi.org/10.1201/9781315375199

Mathot S, Anelli G, Atieh S, Bilton A, Bulat B, Callamand T, Calvo S, Favre G, Geisser JM, Gerardin A, Grudiev A, Lombardi A, Montesinos E, Motschmann F, Pommerenke H, Richerot P, Scibor K, Timmins M, Vretenar M, Taccetti F, Benetti F, Castelli L, Chiari M, Czelusniak C, Falciano S, Fedi M, Mandò PA, Manetti M, Matacotta C, Previtali E, Ruberto C, Virgili V, Giuntini L (2019) The CERN PIXE-RFQ, a transportable proton accelerator for the MACHINA project. Nucl Instr Meth B 459:153–157. https://doi.org/10.1016/j.nimb.2019.08.025

Merlino S (2013) X-ray diffraction and the development of the mineral crystal chemistry. Rend Fis Acc Lincei 24:33–46. https://doi.org/10.1007/s12210-012-0196-y

Morigi MP, Casali F (2018) Radiography and computed tomography for works of art. In: Russo P (ed) Handbook of X-ray imaging: physics and technology. CRC Press, Abingdon, pp 1181–1206. https://doi.org/10.1002/mp.14041

Ngo TD, Kashani A, Imbalzano G, Nguyen KTQ, Hui D (2018) Additive manufacturing (3D printing): a review of materials, methods, applications and challenges. Compos Part B Eng 143:172–196. https://doi.org/10.1016/j.compositesb.2018.02.012

Olsén J, Shen Z, Liu L, Koptyug A, Rännar L-E (2018) Micro- and macro-structural heterogeneities in 316L stainless steel prepared by electron-beam melting. Mater Char 141:1–7. https://doi.org/10.1016/j.matchar.2018.04.026

Opatová K, Zetková I, Kučerová L (2020) Relationship between the size and inner structure of particles of virgin and re-used MS1 maraging steel powder for additive manufacturing. Materials 13:956. https://doi.org/10.3390/ma13040956

Perry MEJ, Griffiths RJ, Garcia D, Sietins JM, Zhu Y, Yu HZ (2020) Morphological and microstructural investigation of the non-planar interface formed in solid-state metal additive manufacturing by additive friction stir deposition. Addit Manuf 35:101293. https://doi.org/10.1016/j.addma.2020.101293

Povilus AP, Wurden CJ, Vendeiro Z, Baquero-Ruiz M, Fajans J (2014) Vacuum compatibility of 3D-printed materials. J of Vac Sci Tech A 32:033001. https://doi.org/10.1116/1.4873556

Rahman NU, Capuano L, Cabeza S, Feinaeugle M, Garcia-Junceda A, de Rooij MB, Matthews DTA, Walmag G, Gibson I, Römer GRBE (2019) Directed energy deposition and characterization of high-carbon high speed steels. Addit Manuf 30:100838. https://doi.org/10.1016/j.addma.2019.100838

Raj BA, Jappes JTW, Khan MA, Dillibabu V, Brintha NC (2019) Studies on heat treatment and electrochemical behaviour of 3D printed DMLS processed nickel-based superalloy. Appl Phys A 125:722. https://doi.org/10.1007/s00339-019-3019-5

Reevesinsight (2012) Shaping our national competency in additive manufacturing: technology innovation needs analysis conducted by the additive manufacturing special interest group for the technology strategy board. In: TSB Knowledge Transfer Network Special Interest Group on Additive Manufacturing. https://reevesinsight.com/wp-content/uploads/2020/02/26-2012-Natioanl-strategy.pdf. Accessed 29 Mar 2021

Sacco E, Moon SK (2019) Additive manufacturing for space: status and promises. Int J Adv Manuf Tech 105:4123–4146. https://doi.org/10.1007/s00170-019-03786-z

Santisteban J, Edwards L, Steuwer A, Withers PJ (2001) Time-of-flight neutron transmission diffraction. J Appl Cryst 34:289–297. https://doi.org/10.1107/S0021889801003260

Schmidt M, Merklein M, Bourell D, Dimitrov D, Hausotte T, Wegener K, Overmeyer L, Vollertsen F, Levy GN (2017) Laser based additive manufacturing in industry and academia. CIRP Ann 66:561–583. https://doi.org/10.1016/J.CIRP.2017.05.011

Schneider CA, Rasband WS, Eliceiri KW (2012) NIH Image to ImageJ: 25 years of image analysis. Nat Methods 2012(9):671–675. https://doi.org/10.1038/nmeth.2089

Sears VF (1992) Neutron scattering lengths and cross sections. Neutron News 3:26–37. https://doi.org/10.1080/10448639208218770

Shinohara T, Kai T, Oikawa K, Segawa M, Harada M, Nakatani T, Ooi M, Aizawa K, Sato H, Kamiyama T, Yokota H, Sera T, Mochiki K, Kiyanagi Y (2016) Final design of the energy-resolved neutron imaging system "RADEN" at J-PARC. J Phys Conf Ser 746:012007. https://doi.org/10.1088/1742-6596/746/1/012007

Shinohara T, Kai T, Oikawa K, Nakatani T, Segawa M, Hiroi K, Su Y, Ooi M, Harada M, Iikura H, Hayashida H, Parker JD, Matsumoto Y, Kamiyama T, Sato H, Kiyanagi Y (2020) The energy-resolved neutron imaging system, RADEN. Rev Sci Instr 91:043302. https://doi.org/10.1063/1.5136034

Bilheux HZ, McGreevy R, Anderson IS (eds) (2009) Neutron imaging and applications. Springer, Boston. https://doi.org/10.1007/978-0-387-78693-3

Taccetti F, Castelli L, Czelusniak C et al (2019) A multipurpose X-ray fluorescence scanner developed for in situ analysis. Rend Fis Acc Lincei 30:307–322. https://doi.org/10.1007/s12210-018-0756-x

Tan C, Zhou K, Ma W, Zhang P, Liu M, Kuang T (2017) Microstructural evolution, nanoprecipitation behavior and mechanical properties of selective laser melted high-performance grade 300 maraging steel. Mater Des 134:23–34. https://doi.org/10.1016/j.matdes.2017.08.026

Tewari R, Mazumder S, Batra IS, Dey GK, Banerjee S (2000) Precipitation in 18 wt% Ni maraging steel of grade 350. Acta Mater 48:1187–1200. https://doi.org/10.1016/S1359-6454(99)00370-5

Thompson A, Maskery I, Leach RK (2016) X-ray computed tomography for additive manufacturing: a review. Meas Sci Technol 27:072001. https://doi.org/10.1088/0957-0233/27/7/072001

Thompson A, McNally D, Maskery I, Leach RK (2017) X-ray computed tomography and additive manufacturing in medicine: a review. Int J Metrol Qual Eng 8:17. https://doi.org/10.1051/ijmqe/2017015

Tremsin AS, Gao Y, Dial LC, Grazzi F, Shinohara T (2016) Investigation of microstructure in additive manufactured Inconel 625 by spatially resolved neutron transmission spectroscopy. Sci Tech Adv Mater 17:324–336. https://doi.org/10.1080/14686996.2016.1190261

Turk C, Zunko H, Aumayr C, Leitner H, Kapp M (2019) Advances in maraging steels for additive manufacturing, weiterentwicklung von maraging-stählen für additive fertigung, BHM Berg und hüttenmännische. Monatshefte 164:112–116. https://doi.org/10.1007/s00501-019-0835-z

Vlassenbroeck J, Masschaele B, Cnudde V, Dierick M, Pieters K, Van Hoorebeke L, Jacobs P (2006) Octopus 8: a high performance tomographic reconstruction package for X-ray Tube and Synchrotron micro-CT, in advances in X-ray tomography for geomaterials, Aussois, France, pp 167–173. https://doi.org/10.1002/9780470612187.ch13

Vontobel P, Lehmann EH, Hassanein R, Frei G (2006) Neutron tomography: method and applications. Phys B 385–386:475–480. https://doi.org/10.1134/S1547477116030146

Watkins T, Bilheux H, An K, Brice C, Payzant E, Dehoff R, Duty C, Blue C, Peter W (2013) Neutron characterization for additive manufacturing. Adv Mater Processes 171:23–27. https://doi.org/10.3390/jimaging3040058

Windsor CG (1981) Pulsed neutron scattering. Taylor and Francis, London

Wong KV, Hernandez A (2012) A Review of additive manufacturing. ISRN Mech Eng 2012:208760. https://doi.org/10.5402/2012/208760

Woo TH (2016) Feasibility study for radiation therapy using nano-robotics incorporated with three-dimensional (3D) printing. Rend Fis Acc Lincei 27:721–728. https://doi.org/10.1007/s12210-016-0559-x

Xu X, Ganguly S, Ding J, Guo S, Williams S, Martina F (2018) Microstructural evolution and mechanical properties of maraging steel produced by wire + arc additive manufacture process. Mater Char 143:152–162. https://doi.org/10.1016/j.matchar.2017.12.002

Yap CY, Chua CK, Dong ZL, Liu ZH, Zhang DQ, Loh LE, Sing SL (2015) Review of selective laser melting: materials and applications. Appl Phys Rev 2:041101. https://doi.org/10.1063/1.4935926

Authors and Affiliations

Francesco Grazzi[1,2] · Carlo Cialdai[1] · Marco Manetti[1] · Mirko Massi[1] · Maria Pia Morigi[3,4] · Matteo Bettuzzi[3,4] · Rosa Brancaccio[3,4] · Fauzia Albertin[3,4,5] · Takenao Shinohara[6] · Tetsuya Kai[6] · Anna Fedrigo[7] · Adriano Di Giovanni[8] · Francesco Arneodo[8] · Rodrigo Torres[8] · Oraib Al-Ketan[8] · Jumaanah Elhashemi[8] · Francesco Taccetti[1] · Lorenzo Giuntini[1,9]

Carlo Cialdai
carlo.cialdai@fi.infn.it

Marco Manetti
marco.manetti@fi.infn.it

Mirko Massi
massi@fi.infn.it

Maria Pia Morigi
mariapia.morigi@unibo.it

Matteo Bettuzzi
matteo.bettuzzi@unibo.it

Rosa Brancaccio
rosa.brancaccio@unibo.it

Fauzia Albertin
fauzia.albertin@unibo.it

Takenao Shinohara
takenao.shinohara@j-parc.jp

Tetsuya Kai
tetsuya.kai@j-parc.jp

Anna Fedrigo
anna.fedrigo@stfc.ac.uk

Adriano Di Giovanni
adg11@nyu.edu

Francesco Arneodo
francesco.arneodo@nyu.edu

Rodrigo Torres
rodrigo.torres@nyu.edu

Oraib Al-Ketan
oga2@nyu.edu

Jumaanah Elhashemi
jumaanah@nyu.edu

Francesco Taccetti
francesco.taccetti@fi.infn.it

[1] Istituto Nazionale di Fisica Nucleare (INFN), Sezione di Firenze, Via G. Sansone 1, Sesto Fiorentino, 50019 Florence, Italy

[2] Consiglio Nazionale delle Ricerche, Istituto di Fisica Applicata "Nello Carrara", 50019 Sesto Fiorentino, Italy

[3] Dipartimento di Fisica e Astronomia "Augusto Righi", Università di Bologna, Viale Berti Pichat 6/2, 40127 Bologna, Italy

[4] Istituto Nazionale di Fisica Nucleare (INFN), Sezione di Bologna, Viale Berti Pichat 6/2, 40127 Bologna, Italy

[5] Study and Research Center Enrico Fermi, Piazza del Viminale 1, 00184 Rome, Italy

[6] Japan Atomic Energy Agency, Tokai-mura, Naka-gun, Ibaraki, Japan

[7] UKRI-STFC, ISIS Neutron and Muon Source, Oxfordshire OX110QX, UK

[8] New York University Abu Dhabi, Abu Dhabi, United Arab Emirates

[9] Dipartimento di Fisica e Astronomia, Università di Firenze, Via G. Sansone 1, Sesto Fiorentino, 50019 Florence, Italy

Journal:	**12210**
Article:	**994**

Author Query Form

Please ensure you fill out your response to the queries raised below and return this form along with your corrections

Dear Author

During the process of typesetting your article, the following queries have arisen. Please check your typeset proof carefully against the queries listed below and mark the necessary changes either directly on the proof/online grid or in the 'Author's response' area provided below

Query	Details Required	Author's Response
AQ1	As per the information provided by the publisher, Figs. (1, 10, 12) will be black and white in print; hence, please confirm whether we can add "colour figure online" to the caption.	
AQ2	Reference 'Tremsin et al. (2016).' is given in list but not cited in text. Please cite in text or delete from list.	
AQ3	Kindly provide necessary details for the Ref. (Kak and Slaney 2001), if possible.	